CrossMark

ORIGINAL ARTICLE

Development and experimental validation of a water gas shift kinetic model for Fe-/Cr-based catalysts processing product gas from biomass steam gasification

Michael Kraussler[1,2] · Hermann Hofbauer[2]

ABSTRACT This paper introduces an improved kinetic model for the water gas shift reaction catalyzed by an Fe-/Cr-based catalyst. The improved model is based on a former model which was developed previously in order to consider the composition and the catalyst poisons (H_2S) of product gas derived from dual fluidized bed biomass steam gasification.

$$r(\varphi_i, T) = 117.8 \, \frac{mol}{g \, Pa^{1.71} \, s} \cdot exp\left(\frac{-126.6 \, \frac{kJ}{mol}}{R.T}\right) \cdot \frac{p_{CO}^{1.77} \cdot p_{H2O}^{0.23} \cdot p_{CO2}^{-0.17} \cdot p_{H2}^{-0.12}}{\left(1 - \frac{K_{MAL}}{K_g}\right)}.$$

Furthermore, this improved model has been validated with experimental data. The data was generated by a WGS reactor which employed a commercial Fe-/Cr-based catalyst and which processed real product gas from the dual fluidized bed biomass steam gasification plant in Oberwart, Austria. Basically, the validation showed good agreement of the measured and the calculated values for the gas composition (absolute errors of the volumetric fractions of up to 1.5 %) and the temperature profile (absolute errors of up to 21 °C) of the WGS reactor. Of all considered gas components, the CO concentration showed the highest error.

The results qualify the improved kinetic model for basic design and engineering of a WGS reactor employing a commercial Fe-/Cr-based catalyst which processes product gas from an industrial scale biomass steam gasification plant.

✉ Michael Kraussler
michael.kraussler@bioenergy2020.eu

[1] Bioenergy2020+ GmbH, Wienerstraße 49, 7540 Güssing, Austria

[2] Institute of Chemical Engineering, TU Wien, Getreidemarkt 9, 1060 Wien, Austria

1 Introduction

The water gas shift (WGS) reaction (see Eq. 1) is a proven method for increasing the hydrogen content in a product gas generated by gasification. Recent research has extensively investigated a WGS unit, employing a commercial Fe-/Cr-based catalyst, which processed product gas from dual fluidized bed (DFB) biomass steam gasification [8, 16, 17].

$$CO + H_2O \leftrightarrow H_2 + CO_2 \quad \Delta H = -41.1 \text{ kJ } mol^{-1} \qquad (1)$$

Since the first applications of the WGS reaction catalyzed by an Fe-/Cr-based catalyst (compare [23]), several kinetic models, based on power laws, have been proposed by different authors, for example, in [2, 3, 9, 13, 20] and [22]. However, most of the investigations of Fe-/Cr-based WGS catalysts were carried out for product gas derived from coal gasification [10, 11]. Zhu and Wachs [28] give a comprehensive summary about kinetic models of the WGS reaction catalyzed by Fe-/Cr-based catalysts.

In addition, Fail [7] proposed a kinetic model for the WGS reaction catalyzed by an Fe-/Cr-based catalyst. This kinetic model specifically takes the product gas from DFB biomass steam gasification into account. In the present paper, this model is referred to as the former kinetic model.

The main gas components of the product gas are H_2, CO, CO_2, and CH_4 which makes the product gas a suitable source for different synthesis reactions, for example, see [19, 21] and [24]. In addition, it contains about 100 cm^3 m^{-3} H_2S. This H_2S

 Springer

content was considered within the former model because H_2S could lead to a performance decrease of the catalyst [26].

In [15], the former model was validated with experimental data from a WGS reactor which employed commercial Fe-/Cr-based catalyst disks (diameter about 6 mm and height about 3 mm, original size) and which processed real product gas from the industrial scale DFB biomass steam gasification plant in Oberwart, Austria. The validation showed significant inaccuracies of the temperature profile along the WGS reactor, which could be attributed to the fact that the former model was established with a milled Fe-/Cr-based catalyst, which did not have the original disk size. Therefore, a higher catalyst surface was available during the establishment of the former kinetic model compared to the validation experiments where the catalyst was used in its original size. However, the WGS reactor, which is located at the site of the gasification plant in Oberwart employed the catalyst in its original pellet size. Consequently, the differences between the measured and calculated temperature profile occurred.

The present paper improves the former kinetic model in order to obtain a better agreement between the experimental data and the model. Consequently, the improved kinetic model should be accurate enough to be used for basic design and engineering of WGS reactors employing Fe/Cr based catalysts which process product gas from DFB biomass steam gasification.

2 Materials and methods

First, this section presents the former kinetic model, which is based on the previous work carried out by Fail (see [7]) and which is improved in the present paper. Second, the experimental setup which generated the data material which was used to improve the former and to validate the improved kinetic model is presented. Third, the derivation of the numerical mass and energy balances of the WGS reactor is introduced, which enables the comparison of the measured data with the results of the model.

2.1 The former kinetic model

This paper is based on a kinetic model which was derived at the TU Wien from results obtained with a laboratory scale chemical kinetics test rig (see [7]). For that kinetic model, the Fe-/Cr-based catalyst was milled before the kinetic parameters were determined. Consequently, the model shows inaccuracies regarding the reaction rate and, therefore, the temperature profile (compare [15]) if the catalyst is used in its original size.

In this paper, the former kinetic model has been improved in order to meet the requirements for using this model for the

basic design and engineering of a WGS reactor which processes product gas from DFB biomass steam gasification.

The starting point for both the former and the improved kinetic model was the power law in Eq. 2 which is based on [7] and [15]:

$$r(\varphi_i, T) = k_0 \cdot exp\left(\frac{-E_a}{R \cdot T}\right) \cdot p_{CO}^a \cdot p_{H2O}^b \cdot p_{CO2}^c \cdot p_{H2}^d \cdot \left(1 - \frac{K_{MAL}}{K_g}\right) \tag{2}$$

The reaction rate $r(\varphi_i, T)$ is a function of the reactive species (CO, H_2O, CO_2, and H_2) and the temperature. Other gas components which are usually contained in small amounts in the product gas of the DFB biomass steam gasification are considered as inert.

The parameters which describe the reaction rate are the rate constant k_0, the activation energy E_a, and the reaction exponents (a, b, c, and d) of each component i which is a reactant of the WGS reaction (see Eq. 1). p_i is the partial pressure, R is the general gas constant, and T is the temperature along the reactor. K_{MAL} is the mass action law and K_g the equilibrium constant calculated from thermo-physical properties.

$$K_{MAL} = \frac{\varphi_{H2} \cdot \varphi_{CO2}}{\varphi_{CO} \cdot \varphi_{H2O}} \tag{3}$$

$$K_g = exp\left(\frac{-\Delta G(T)}{R \cdot T}\right) \tag{4}$$

The partial pressure of each component p_i can be expressed by the overall absolute pressure p and the volumetric fraction φ_i.

$$p_i = \varphi_i \cdot p \tag{5}$$

The work in [7] led to the following parameters for Eq. 2, resulting in the former model (see Table 1).

2.2 Setup for the generation of the experimental data

This section provides information about the plants and the measurement principles which were used for the data

Table 1 Parameters of the former kinetic model (see [7] and [15])

Parameters	Values	Units
k_0	117.8	mol g^{-1} Pa$^{-(a+b+c+d)}$ s^{-1}
E_a	101.9	kJ mol^{-1}
a	1.77	–
b	0.23	–
c	−0.17	–
d	−0.12	–

generation in order to improve the former and to validate the improved kinetic model.

2.2.1 The dual fluidized bed steam gasification plant

The product gas for the WGS reactor was extracted from the commercial DFB biomass steam gasification plant in Oberwart, Austria. The gasification plant is operated as combined heat and power (CHP) plant and generates electricity and heat for the district. Figure 1 shows a simplified flowchart of the gasification plant.

For the improvement of the former and the validation of the improved kinetic model, the product gas was extracted from two extraction points (see also Fig. 1). The first extraction point was located before the rapeseed methyl ester (RME) gas scrubber, and the second extraction point was located after the RME gas scrubber. The product gas which was extracted before the RME gas scrubber showed a significantly higher amount of tar (about 10 $g\ m^{-3}$) and steam (about 35 %) compared to the product gas which was extracted after the RME gas scrubber (about 2 $g\ m^{-3}$ tar and about 7 % steam).

Further details of the plant can be found in [6, 15–17].

2.2.2 The water gas shift reactor

Figure 2 shows a simplified flowchart of the cylindrical WGS reactor located at the site of the gasification plant in Oberwart which was used for the generation of the experimental data.

The WGS reactor successively processed a partial flow of the product gas of the gasification plant from the two extraction points (see Fig. 1). The product gas was mixed with additional steam which was provided by a steam generator. The gas inlet temperature was adjusted with a heating section to about 350 °C. At the bottom of the reactor, a screen plate was used for carrying the commercial Fe-/Cr-based catalyst which had been in operation for more than 2000 h at the time this research was conducted. The catalyst bed was a fixed bed with a diameter of 9 cm and a height of about 40 cm resulting in a catalyst bed volume of about 2.5 dm^3. The bulk density of the catalyst bed was 1.24 $kg\ dm^{-3}$. The wall thickness of the reactor was 3 mm and the insulation consisted of stone wool with a thickness of 10 cm and a thin layer of Al around the outer surface.

Seven thermocouples were used to measure and to record the temperature profile along the WGS reactor. The temperature profile allowed reaching some conclusion about the
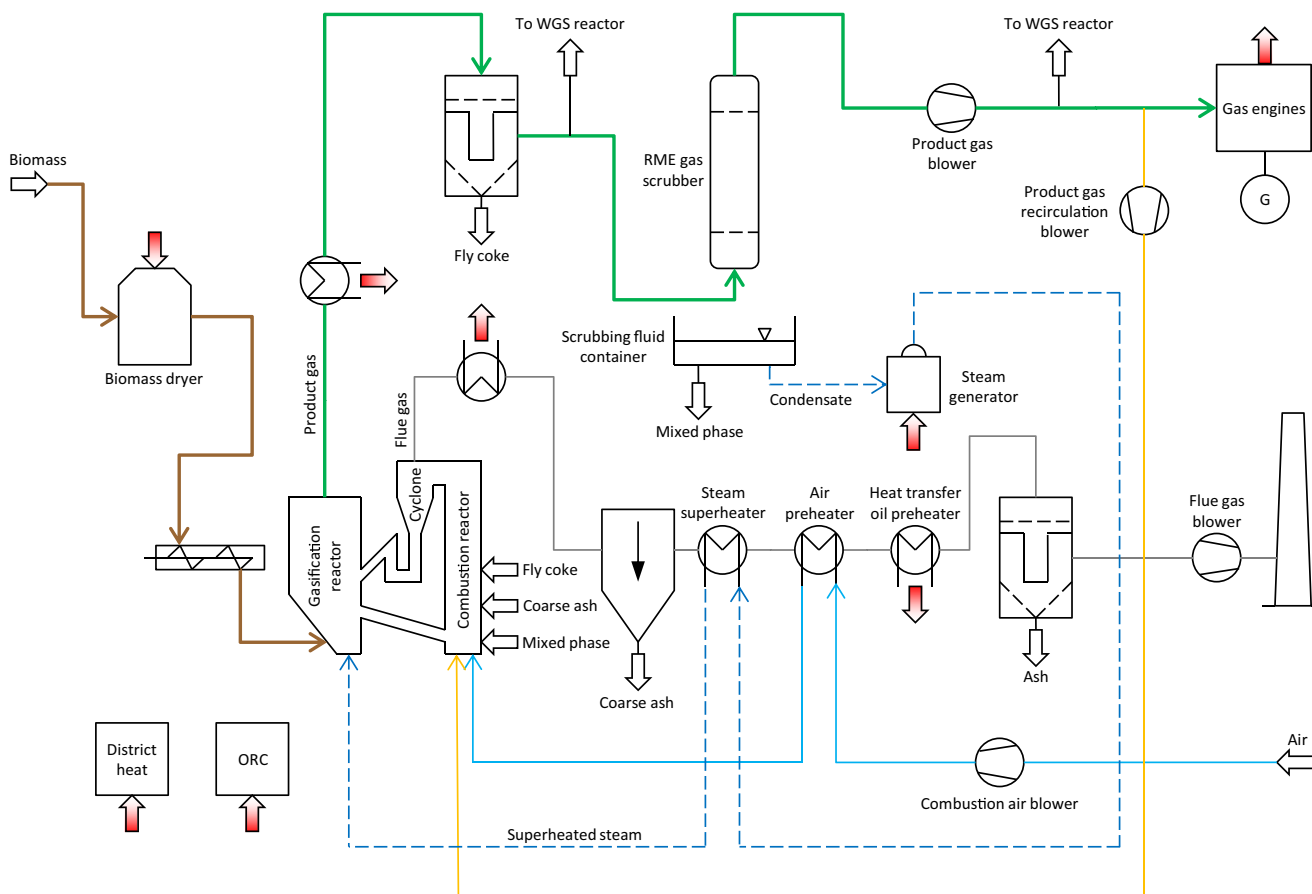

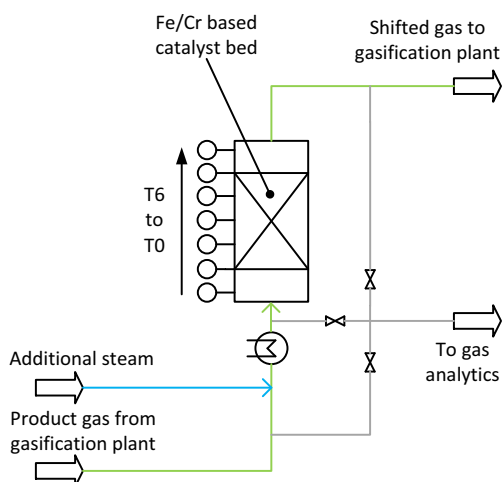**Fig. 1** Simplified flowchart of the gasification plant in Oberwart, Austria

Fig. 2 Simplified flowchart of the WGS reactor which was used for the generation of the experimental data

Fig. 3 Setup of the gas conditioning before the GC and the water content determination

activity of the commercial Fe-/Cr-based catalyst due to the exothermic nature of the WGS reaction.

After the product gas was processed in the reactor, it was recycled back to the gasification plant. A sample flow of the processed gas extracted before the steam addition, before the inlet, and after the outlet of the WGS reactor was sent to the analytical line and, subsequently, to a gas chromatograph (GC) in order to measure the dry gas composition of the processed gas.

The WGS reactor operated at ambient pressure and the pressure drop along the catalyst bed was between 500 and 1000 Pa during the whole operating time.

2.2.3 Measurement of the temperature profile along the water gas shift reactor

Figure 2 shows the positions of the thermocouples (type J) along the WGS reactor. Thermocouple T0 was positioned before the fixed bed Fe-/Cr-based catalyst. Therefore, it was not in the reactive zone. T1 to T5 were positioned along the catalyst bed at a distance of 10 cm from each other. T1 was positioned right at the beginning of the catalyst bed, and T5 was positioned right at the end of the catalyst bed. T6 was outside the catalyst bed. T1 to T5 enabled the measurement and recording of the temperature profile along the fixed bed WGS catalyst.

2.2.4 Measurement of the gas composition at the inlet and the outlet of the water gas shift reactor

Figure 3 shows the setup of the gas conditioning before the gas chromatograph (GC) that was used for the determination of the gas composition.

Before entering the GC, the gas stream passed through two gas washing bottles filled with glycol at a temperature of about
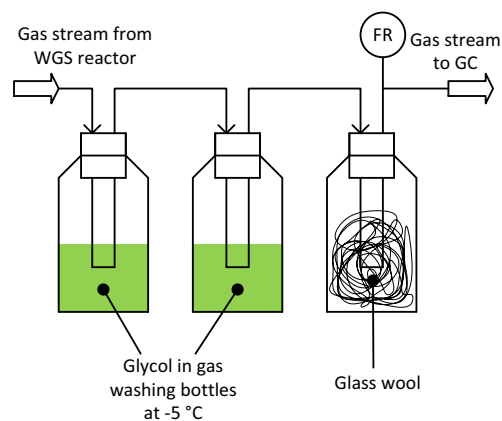
−5 °C in order to condense and separate the steam. Therefore, a dry gas stream could be assumed after the gas washing bottles. The dry gas stream passed through another gas washing bottle filled with glass wool in order to prevent aerosols from entering the GC. After the glass wool bottle, a gas meter recorded the volumetric dry gas flow.

The steam content in the product gas before the addition of steam, before the inlet of the reactor, and after the outlet of the reactor was determined with a gravimetrical method. The wet gas stream passed through the gas washing bottles for a certain time, where the steam was condensed. Subsequently, the volumetric dry gas flow was recorded and the gas washing bottles were weighed. Consequently, the steam content before the steam addition, before the inlet, and before the outlet of the reactor could be determined.

The volumetric dry gas flow rate at the inlet of the WGS reactor was calculated by the water balance of the steam generator according to the following equation and the known volumetric flow rate of the steam addition:

$$\dot{V}_{Dry} = \dot{V}_{Wet,In} \cdot \left(1 - \varphi_{H2O,In}\right)$$
$$= \frac{\left(\dot{V}_{H2O,Add} \cdot \varphi_{H2O,Out} - \dot{V}_{H2O,Add}\right)}{\left(\varphi_{H2O,In} - \varphi_{H2O,Out}\right)} \cdot \left(1 - \varphi_{H2O,In.}\right)$$

In this paper, all volumetric gas flow rates and gas volumes are given at standard temperature and pressure (STP, 273.15 K and 101325 Pa).

A GC (Clarus 500™ from Perkin Elmer) was used to measure the gas composition at the inlet and at the outlet of the WGS reactor. A thermal conductivity detector (TCD) enabled the quantification of the CO, CO_2, CH_4, N_2, and higher hydrocarbons in the gas stream with two different columns (7' HayeSep N, 60/80 1/8" SF and 9' molecular sieve 13× 45/60, 1/8" SF). The higher hydrocarbons were considered inert and, therefore, their amount was added to the N_2 concentration. The GC was not able to measure the H_2 concentration.

Consequently, the H_2 concentration was calculated by closing the overall mass balance. Furthermore, CH_4 was also considered inert for the modeling process.

In addition, the measurements were validated by applying the least squares method on the elemental balances of C, H, O, and N describing the WGS reactor.

2.3 Balances and consideration of the heat losses of the water gas shift reactor

This section describes the derivation of the numerical molar and energy balances of the WGS reactor which was used for gathering the experimental data. Furthermore, the approach for the consideration of the heat losses along the reactor is shown.

For the derivation of the balances, the assumption of an ideal plug flow reactor was made.

2.3.1 Molar balance of the water gas shift reactor

Figure 4 shows the derivation of the molar balance of the WGS reactor.

The molar balance of each reactive component i leads to

$$\dot{n}_i(z + \Delta z) - \dot{n}_i(z) = \pm r(\varphi_i, T) \cdot \rho_s \cdot \Delta z \cdot A. \tag{6}$$

$\dot{n}_i$ is the molar flow of component i and A is the cross section of the catalyst bed. ρ_s is the bulk density of the Fe-/Cr-based catalyst and Δz is the grid step, which was chosen with 1 mm. $\pm$ indicates whether component i is an educt or a product of the WGS reaction.

The limiting process $\lim \Delta z \to 0$ leads to the following differential equation:

$$\frac{d\dot{n}_i}{dz} = \pm r(\varphi_i, T) \cdot \rho_s \cdot A. \tag{7}$$

Replacing the molar flow rate $\dot{n}_i$ of each component i with the overall molar flow rate $\dot{n}$ and the volumetric fractions of each component i leads to

$$\frac{d\varphi_i}{dz} = \pm r(\varphi_i, T) \cdot \rho_s \cdot A \cdot \frac{1}{\dot{n}}. \tag{8}$$

This step is valid because of the equimolar character of the WGS reaction and the assumption of ideal gas behavior.

Using the finite difference approach (see [25]) leads to

$$\varphi_i^{K+1} = \pm r(\varphi_i^K, T^K) \cdot \rho_s \cdot A \cdot \frac{1}{\dot{n}} \cdot \Delta z + \varphi_i^K. \tag{9}$$

Equation 9 enables the calculation of the concentration profiles of CO, H_2O, CO_2, and H_2 along the catalyst bed height of the WGS reactor.
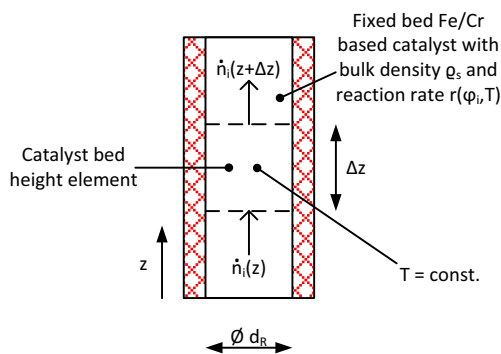

Fig. 4 Illustration for the calculation of the molar balance for the WGS reactor

2.3.2 Energy balance of the water gas shift reactor

Figure 5 shows a drawing for the derivation of the energy balance of the WGS reactor.

The energy balance of the differential height element leads to

$$\dot{h}(z + \Delta z) - \dot{h}(z)$$
$$= \pm \Delta h_R(\varphi_i, T) \cdot r(\varphi_i, T) \cdot \rho_s \cdot A \cdot \Delta z - \Delta \dot{Q}(z). \tag{10}$$

Here, $\Delta h_R(\varphi_i, T)$ is the formation enthalpy of the WGS reaction, $\dot{h}$ is the overall enthalpy flow, and $\Delta \dot{Q}(z)$ is the term which describes the heat losses along each height element Δz. The limiting process $\lim \Delta z \to 0$ and the overall molar heat capacity $c_P(\varphi_i, T)$ of the gas stream lead to

$$\frac{dT}{dz} = \pm \Delta h_R(\varphi_i, T) \cdot r(\varphi_i, T) \cdot \frac{\rho_s \cdot A}{c_P(\varphi_i, T) \cdot \dot{n}} - \frac{d\dot{Q}(z)}{c_P(\varphi_i, T) \cdot \dot{n} \cdot dz}. \tag{11}$$

Applying the finite difference approach to Eq. 11 leads to

$$T^{K+1} = \pm \Delta h_R(\varphi_i^K, T^K) \cdot r(\varphi_i^K, T^K) \cdot \frac{\rho_s \cdot A}{c_P(\varphi_i, T) \cdot \dot{n}} \cdot \Delta z - \frac{\Delta \dot{Q}^K}{c_P(\varphi_i^K, T^K) \cdot \dot{n}} + T^K. \tag{12}$$

Equation 12 enables the calculation of the temperature profile along the catalyst bed height of the WGS reactor. It also considers the heat losses which occur along the WGS reactor.

Equations 9 and 12 form a system of equations which describes the concentration and temperature profiles along the WGS reactor. This system of equations was solved using an algorithm which was written with the numerical software Scilab™ [27].

The thermo-physical properties of the product gas components were calculated by NASA polynomials [18].
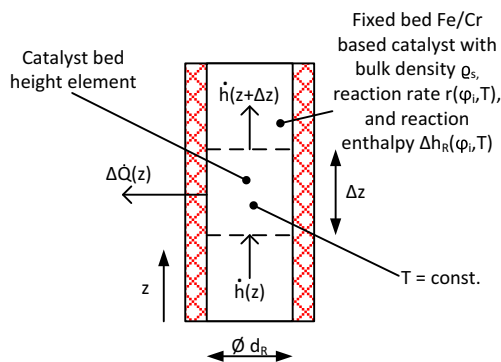
Fig. 5 Illustration for the calculation of the energy balance for the WGS reactor

The input values for the numerical solution are the volumetric steam flow rate $\dot{V}_{H2O}$, the volumetric dry gas flow rate $\dot{V}_{Dry}$, the kinetic model coefficients, the reactor geometry, the gas composition at the reactor inlet φ_i^0, the reactor inlet temperature T^0, and the ambient temperature T_0.

With the numerical calculation of the mass and energy balance of the WGS reactor, the former kinetic model (see Table 1) was improved and the resulting improved kinetic model (see Table 3) was validated with experimental data. To acquire the experimental data, the WGS reactor was operated with real product gas from the gasification plant.

2.3.3 Consideration of the heat losses along the water gas shift reactor

The heat losses along the WGS reactor were considered because they have a significant influence on the energy balance of the WGS reactor.

The heat losses $\Delta\dot{Q}(z)$ are calculated for each Δz along the WGS reactor according to

$$\Delta\dot{Q}(z) = (T(z) - T_0).R_Q(z). \tag{13}$$

Using the finite difference approach leads to

$$\Delta\dot{Q}^K = \left(T^K - T_0\right) \cdot R_Q^K. \tag{14}$$

Here, $T(z)$ is the actual reactor temperature for each z, T_0 is the ambient temperature, and $R_Q(z)$ is the overall heat transfer conductivity for each z; it can be described by four different single heat transfer conductivity

coefficients (ambient, insulation, reactor wall, and inner reactor) according to Eq. 15.

$$\frac{1}{R_Q} = \frac{1}{\alpha_0 \cdot A_0} + \frac{\delta_I}{\lambda_I \cdot A_I} + \frac{\delta_S}{\lambda_S \cdot A_S} + \frac{1}{\alpha_R \cdot A_R}$$

$$= \frac{1}{\pi \cdot \Delta z} \cdot \left(\frac{1}{\alpha_0 \cdot d_0} + \frac{\delta_I}{\lambda_I \cdot \frac{d_I - d_S}{ln\left(\frac{d_I}{d_S}\right)}} + \frac{\delta_S}{\lambda_S \cdot \frac{d_S - d_R}{ln\left(\frac{d_S}{d_R}\right)}} + \frac{1}{\alpha_R \cdot d_R} \right)$$

$$\tag{15}$$

These four terms describe the heat transfer conductivity of the shell of the reactor (compare Fig. 6). The heat losses of the bottom surface and the top surface of the reactor are neglected because the surfaces are significantly smaller than the shell surface.

In the following, the derivation of the four heat transfer conductivity terms (ambient, insulation, reactor wall, and inner reactor) is shown.

Ambient This term consists of the heat transfer coefficients α_0 and the outer surface of the reactor A_0.

α_0 can be calculated with the heat transfer coefficient caused by the radiation emitted by the insulation surface (α_{Rad}, thin Al layer) and the heat transfer coefficient caused by natural convection (α_{Conv}):

$$\alpha_0 = \alpha_{Rad} + \alpha_{Conv} \tag{16}$$

According to [1], α_{Rad} can be calculated with Eq. 17.

$$\alpha_{Rad} = \epsilon_0 \cdot \sigma \cdot \frac{T_S^4 - T_0^4}{T_S - T_0} =$$

$$= 0.09 \cdot 5.67 \cdot 10^8 \frac{W}{m^2 \cdot K^4} \cdot \frac{((50 + 273.15)K)^4 - ((25 + 273.15)K)^4}{(50 + 273.15)K - (25 + 273.15)K} \tag{17}$$

$$= 0.61 \frac{W}{m^2 \cdot K}$$

The convective heat transfer coefficient α_{Conv} can be calculated by the Nusselt number Nu with the correlation in Eq. 18 (see [5]).

$$Nu = \frac{\alpha_{Conv} \cdot d_0}{\lambda}$$

$$= \left\{ 0.6 + \frac{0.387 \cdot (Gr \cdot Pr)^{\frac{1}{6}}}{\left[1 + (0.559 \cdot Pr^{-1})^{\frac{9}{16}}\right]^{\frac{8}{27}}} \right\}^2 \tag{18}$$

In this equation, d_0 is the outer diameter of the reactor and λ is the heat conductivity of air.

The Grashof number Gr with the gravitational constant g, the thermal expansion coefficient of air β, the

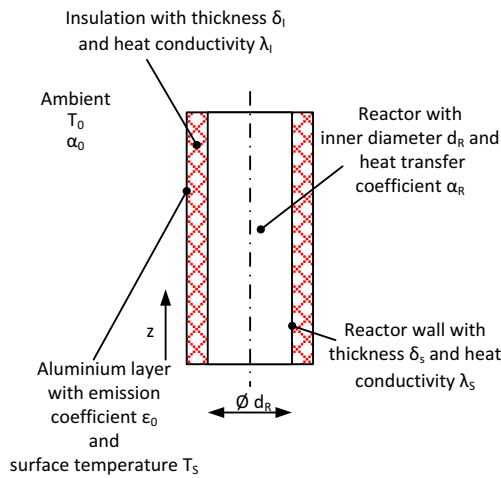**Fig. 6** Drawing for the consideration of the heat losses along the reactor shell

outer reactor diameter d_0, and the kinematic viscosity of air ν

$$Gr = \frac{g \cdot \beta \cdot (T_S - T_0) \cdot d_0^3}{\nu^2}$$

$$= \frac{9.81 \frac{m}{s^2} \cdot \frac{1}{(25 + 273.15)} \frac{1}{K} \cdot (25\,K) \cdot 0.296^3\,m^3}{\left(1.6 \cdot 10^{-5}\right)^2 \left(\frac{m^2}{s}\right)^2} \quad (19)$$

$$= 8.33 \cdot 10^7$$

and the Prandtl number of air
Pr = 0.7
lead to
Nu = 47.89
and, consequently, to

$$\alpha_{Conv} = \frac{Nu \cdot \lambda}{d_0} = \frac{47.89 \cdot 2.6 \cdot 10^{-2} \frac{W}{m \cdot K}}{0.296\,m} = 4.21 \frac{W}{m^2 \cdot K}. \quad (20)$$

With Eqs. 17 and 20, the overall heat transfer coefficient for the ambient can be calculated with

$$\alpha_0 = \alpha_{Rad} + \alpha_{Conv} =$$
$$= 0.61 \frac{W}{m^2 \cdot K} + 4.21 \frac{W}{m^2 \cdot K} = 4.82 \frac{W}{m^2 \cdot K} \quad (21)$$

It can be seen that the heat transfer coefficient which is caused by the natural convection is about seven times higher than the heat transfer coefficient of the radiation at this low ambient temperature.

Furthermore, the outer surface of the reactor can be calculated with

$$A_0 = d_0 \cdot \pi \cdot \Delta z \quad (22)$$

Insulation This term consists of the thickness of the insulation δ_I, the heat conductivity of the insulation, λ_I and

the mean logarithmic surface of the insulation A_I. In general, the mean logarithmic surface (A_m) can be calculated using the outer (A_o) and inner (A_i) surface of a cylindrical object according to Eq. 23.

$$A_m = \frac{A_o - A_i}{ln \frac{A_o}{A_i}} \quad (23)$$

Reactor wall This term consists of the thickness of the reactor wall δ_S, the heat conductivity of steel λ_S, and the mean logarithmic surface of the inner reactor A_R and the outer surface of the reactor wall A_S.

Inner reactor The inner reactor is considered as an ideal pipe reactor with the inner surface area A_R. Therefore, [1] (page 418) gives a Nusselt number of Nu = 3.657. With Nu, the inner reactor diameter d_R, and the estimated heat conductivity of the product gas λ_R, the heat transfer coefficient α_R can be calculated.

Hence, the overall heat transfer conductivity R_Q for each Δz is $2.46 \cdot 10^{-4}\ W \cdot K^{-1}$ with the chosen parameters. With this information, the heat losses along the reactor can be calculated according to Eqs. 13 and 14, respectively.

3 Result and discussion

First, this section presents the determination of the parameters for the improved kinetic model. Second, the validation results of the improved kinetic model are discussed.

Table 2 gives an overview of the four different operating points of the WGS reactor (OP1 to OP4). OP1 was used to improve the former kinetic model, and OP2 to OP4 were used for the validation of the improved kinetic model with experimental data from the WGS reactor.

Table 2 Overview of the operating points for the improvement of the kinetic model and its subsequent validation

OP	GHSV	STDGR	$\dot{V}_{Dry}$	Usage
-	h^{-1}	–	$m^3 \cdot h^{-1}$	–
1	495	1.6	1.24	Improvement
2	445	1.9	1.11	Validation
3	326	1.6	0.82	Validation
4	414	1.2	1.04	Validation

The operating conditions of the WGS reactor were described by the gas hourly space velocity (GHSV) and the steam to dry gas ratio (STDGR) in Eqs. 24 and 25.

$$GHSV = \frac{\dot{V}_{Dry}}{V_{Cat}} \qquad (24)$$

$$STDGR = \frac{\dot{V}_{H2O}}{\dot{V}_{Dry}} \qquad (25)$$

OP1, OP2, and OP3 processed product gas which was extracted before the RME gas scrubber of the gasification plant and OP4 processed gas which was extracted after the RME gas scrubber.

3.1 The improved kinetic model

In order to improve the former kinetic model, a new parameter for the activation energy E_a was sought, one that should consider the fact that the catalyst was used in its original pellet size during this experimental approach, which was in contrast to the determination of the former kinetic model, where the catalyst was milled and, therefore showed a higher specific surface. E_a was chosen as the parameter to improve because it significantly affects the temperature profile (compare Eq. 2). To do so, a variation of E_a with subsequent error calculation regarding the temperature profile was done.

For each E_a, the temperature profile along the WGS reactor (thermocouples 1 to 5) was calculated and compared with the measured values of OP1. Subsequently, the overall error for each E_a was calculated according to Eq. 26.

$$Err = \sum_{i=1}^{5} \sqrt{\left(T_{c,i} - T_{m,i}\right)^2} \qquad (26)$$
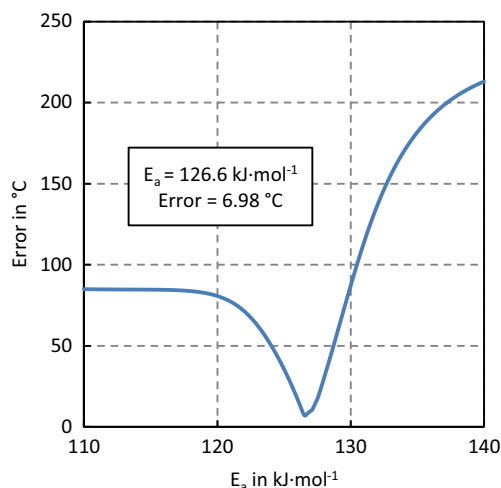
The result can be seen in Fig. 7.

Fig. 7 Variation of E_a with corresponding error for OP1

The new value for $E_{a,j}$ was chosen to be that for which the error Err was a minimum.

The new value of E_a and, consequently, the other parameters for Eq. 2 which were not changed can be seen in Table 3.

Compared to the models in [2, 7, 13, 15] and [22], the activation energy E_a is higher. In these approaches, the activation energy values varied between 95 and 118 kJ mol^{-1}. However, Chinchen et al. [4] give a value of 129.4 kJ mol^{-1} for the activation energy for WGS catalysts used at industrial scale and at pressures of up to 3.0 MPa, which is in good agreement with the value found in this work.

In addition, the presented value of factor a shows that the influence of the CO partial pressure is also higher (1.77 in this work versus about 1.0 in [2, 13], and [22]). This could be explained by the low operating pressure in this work and, therefore, an even lower adsorption of CO on the catalyst surface.

In contrast, the reaction exponents b, c, and d are in the same order of magnitude, which also indicates that the supply of H_2O, CO_2, and H_2 to the catalyst surface is not limiting the reaction.

3.2 Validation of the improved kinetic model with experimental data

The improved kinetic model was validated with temperature measurements and concentration measurements of all four operating points where real product gas from the gasification plant was processed in the WGS reactor.

Figure 8 shows the validation of the kinetic model with the measured temperature profiles along the WGS reactor from all four operating points (OP1 to OP4). The temperatures at T1 were the boundary conditions; therefore, the measurements and the calculations have the same value.

It can be seen that the calculated and measured temperature profiles have nearly no difference at OP1 because the improved model is based on this operating point.

The temperature profiles of OP2 also have a higher difference. However, the calculated profile was slightly lower than the measured profile. Consequently, the chosen activation energy of $E_a = 126.6$ kJ mol^{-1} seems to be too high for OP2.

Table 3 Parameters of the improved kinetic model

Parameters	Values	Units
k_0	117.8	mol g^{-1} $Pa^{-(a+b+c+d)}$ s^{-1}
E_a	126.6	kJ mol^{-1}
a	1.77	–
b	0.23	–
c	−0.17	–
d	−0.12	–

Fig. 8 Temperature profiles along the water gas shift reactor for all four operating points
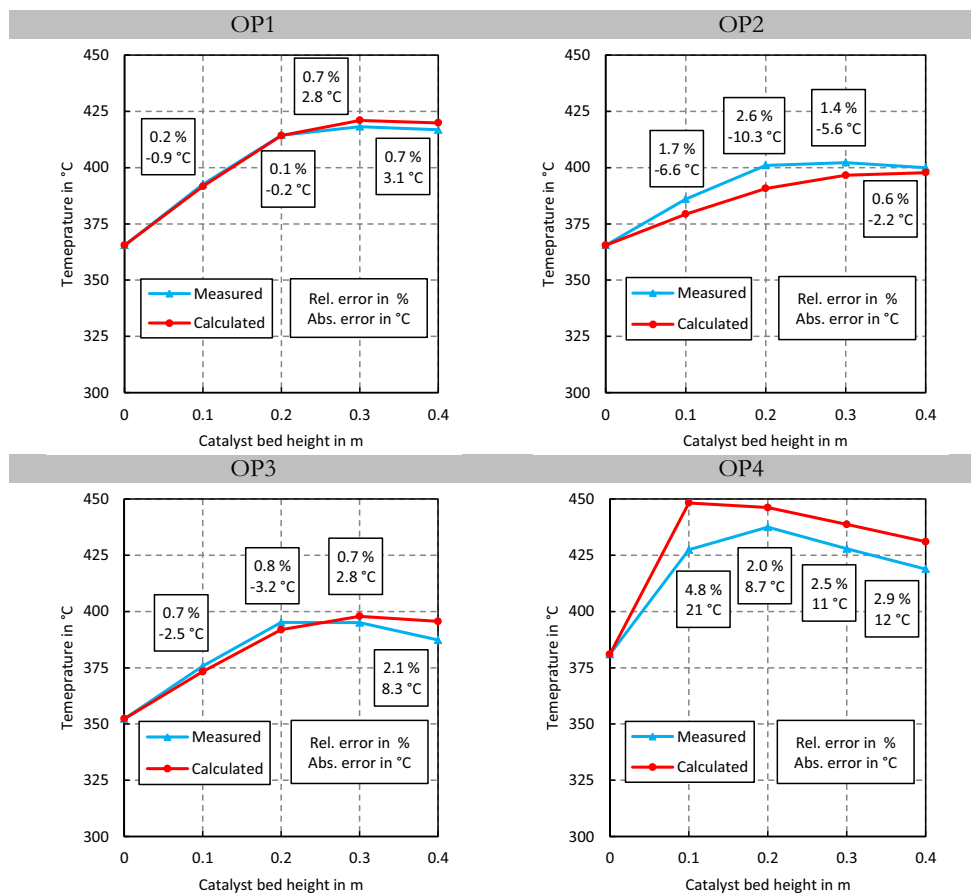
For OP3, the temperature profiles show good agreement for the first three measurement points. However, it seems that the calculated heat losses in the improved model are too low compared to the measured values, which explains the higher calculated temperature profile at measurement points 4 and 5. Consequently, the highest error occurred at the last measurement point.

OP4 shows the highest gap regarding the calculated and the measured temperature profile which could be explained by the fact, that this operating point processed product gas with a lower STDGR of 1.2 compared to the other operating points. For this operating point, the chosen value of E_a was too low, which indicates that a lower STDGR ratio has a negative effect on the kinetics. This is in agreement with Hla et al. [12], where the authors observed that higher steam content increased the reaction rate of the WGS reaction. However, the measurement points 3 to 5 indicate good agreement between the calculated and measured heat losses.

Table 4 shows the calculated and measured values of the gas compositions at the inlet and outlet of the WGS reactor. The measured inlet concentrations were the boundary conditions for the calculation.

Overall, it can be seen that the error of the CO concentration is the highest of all measured and calculated components.

However, the absolute error is quite low, which indicates a good agreement of the measured and calculated values.

Taking a look at OP1, it can be seen that the measured and calculated values show good agreement regarding the concentrations of H_2, CO_2, CH_4, and N_2. The relative error of CO is higher than the relative errors of the other gas components. However, the absolute error is about 1 %.

Looking at OP2, it can be seen that the absolute and relative errors of the CO concentration are slightly higher than for OP1. In addition, OP2 has a higher CO_2 concentration than the CO concentration at the inlet of the WGS reactor which can be attributed to a partial load operation of the gasification plant during this measurement. At partial load operation, a higher steam to fuel ratio leads to higher CO_2 concentrations and, consequently, to lower CO concentrations (compare [14]).

OP3 shows similar results as for OP1. However, the overall errors are higher; especially, the CO concentration shows a higher relative error and a higher absolute error compared to OP1.

OP4 shows, again, good agreement of the measured and calculated concentrations at the outlet of the WGS reactor. It shows again the highest relative error for the CO concentrations. The absolute error of 0.9 % is also in the same order of magnitude as for the other operating points.

Table 4 Concentrations at the inlet and outlet of the WGS reactor for all operating points. The measured reactor inlet concentrations as well as the measured and calculated reactor outlet concentrations are shown. The H_2 concentration of the measurements was calculated by closing the mass balance as H_2 could not be detected by the GC. The measurements were single sample measurements; therefore, no standard deviation can be given

	φ_{H2} %	φ_{CO} %	φ_{CO2} %	φ_{CH4} %	φ_{N2} %
OP1					
Inlet	38.9	25.4	20.7	10.5	4.5
Outlet measured	48.9	3.4	35.0	9.0	3.7
Outlet calculated	49.9	2.9	34.9	8.6	3.7
Rel. error	1.9 %	14.1 %	0.3 %	3.7 %	0.3 %
OP2					
Inlet	37.3	23.0	24.1	10.4	5.2
Outlet measured	46.7	4.4	36.0	9.0	3.9
Outlet calculated	46.4	5.1	35.2	8.9	4.4
Rel. error	0.6 %	17.2 %	2.4 %	1.0 %	12.7 %
OP3					
Inlet	39.8	25.3	21.1	9.5	4.3
Outlet measured	49.8	5.1	33.3	8.4	3.4
Outlet calculated	50.3	3.6	34.8	7.9	3.6
Rel. error	0.8 %	30.0 %	4.5 %	6.6 %	4.7 %
OP4					
Inlet	38.2	23.3	22.7	10.0	5.8
Outlet measured	48.4	3.4	35.2	8.7	4.5
Outlet calculated	48.7	2.5	35.8	8.3	4.8
Rel. error	0.6 %	27.5 %	1.7 %	3.9 %	8.1 %

Fig. 9 Comparison of the temperature profile along the WGS reactor between the measured data, the improved kinetic model, and the former kinetic model using data from OP1

In contrast, the CH_4 and N_2 concentrations of the former and improved are at the same level, which indicates, that CH_4 and N_2 did not take part in a reaction and the error between the measured and calculated values was caused by a measurement error. The small deviation can be explained by the slightly higher volumetric dry gas flow rate if the former kinetic model is employed for the calculation.

4 Conclusion and outlook

In this paper, a former kinetic model for the water gas shift reaction was improved with experimental data from a water gas shift reactor which processed real product gas from dual fluidized bed biomass steam gasification and which employed a commercial Fe-/Cr-based catalyst. Both kinetic models, the former one and the improved one, considered a H_2S amount of about $100 \; cm^3 \; m^{-3}$ which is usually contained in the product

3.3 Comparison of the improved with the former model

In this section, the improved and the former kinetic model are compared by using the experimental data from OP1. Figure 9 shows the comparison of the temperature profile between the measured data, the improved kinetic model, and the former kinetic model.

It can be seen that the temperature profile, which was calculated with the former kinetic model, shows significant deviation compared with the measured data and, therefore, also with the improved kinetic model.

Table 5 shows the comparison of the volumetric fractions of the gas components between the measured data, the improved kinetic model, and the former model.

It can be seen that the former kinetic model shows a higher H_2 and CO_2 concentration and, consequently, a lower CO content. This could be explained by the higher reaction rate of the former kinetic model. In addition, the volumetric fractions of the former kinetic model are very close to the equilibrium composition at the given parameters.
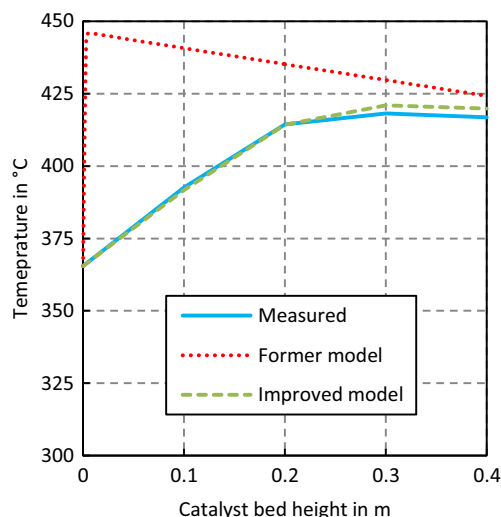
Table 5 Comparison of the volumetric fractions of the gas components between the measured data, the improved kinetic model, and the former model using data from OP1

	φ_{H2} (%)	φ_{CO} (%)	φ_{CO2} (%)	φ_{CH4} (%)	φ_{N2} (%)
Inlet	38.9	25.4	20.7	10.5	4.5
Outlet measured	48.9	3.4	35.0	9.0	3.7
Outlet improved	49.9	2.9	34.9	8.6	3.7
Outlet former	50.5	1.7	35.7	8.5	3.6

gas generated from dual fluidized bed biomass steam gasification.

$$r(\varphi_i, T) = 117.8 \frac{mol}{g \cdot Pa^{1.71} s} \cdot exp\left(\frac{-126.6 \frac{kJ}{mol}}{R \cdot T}\right) \cdot p_{CO}^{1.77} \cdot p_{H2O}^{0.23} \cdot p_{CO2}^{-0.17} \cdot p_{H2}^{-0.12}$$
$$\cdot \left(1 - \frac{K_{MAL}}{K_g}\right)$$

Furthermore, this improved kinetic model was validated with the experimental data from four different operating points of the water gas shift reactor.

In order to enhance the accuracy of the validation, the heat losses of the water gas shift reactor, which play a significant part in the energy balance, were also considered.

For the improvement of the former kinetic model and the validation of the improved kinetic model, the gas composition at the inlet and the outlet of the water gas shift reactor was measured. In addition, the temperature profile along the catalyst bed of the reactor was recorded.

Overall, the validation showed good agreement of the measured and calculated values for the gas compositions and the temperature profiles of the water gas shift reactor. Of all considered gas components, the CO concentration showed the highest error. However, the highest absolute error was about 1.5 % (relative error of 30.0 %). The highest absolute error of the temperature profile was 21 °C (relative error of 4.8 %). In addition, a low steam to dry gas ratio at the reactor inlet (from 1.2 and below), reduced the accuracy of the model.

Hence, these results qualify the presented improved kinetic model for basic design and engineering of a water gas shift reactor which employs a commercial Fe-/Cr-based catalyst and which processes product gas derived from dual fluidized biomass steam gasification if the steam to dry gas ratio at the reactor inlet is set to about 1.5.

Furthermore, future work should focus on an additional kinetic model which considers a product gas which is derived from the gasification of alternative fuels like waste or, for example, plastic residues.

Abs, absolute; BDL, below detection limit; Cat, catalyst; CHP, combined heat and power; d.b., dry basis; DFB, dual fluidized bed; DL, detection limit; FR, flow record; GC, gas chromatograph; OP, operating point; ORC, organic Rankine cycle; Rel, relative; RME, rapeseed methyl ester; STP, standard temperature and pressure (273.15 K and 101325 Pa); TX, thermocouple X along the WGS reactor; TCD, thermal conductivity detector; WGS, water gas shift.

Greek Symbols α_0 Heat transfer coefficient of the outer reactor wall to the ambient in W m^{-2} K^{-1}

α_{Conv} Heat transfer coefficient of the outer reactor wall caused by natural convection in W m^{-2} K^{-1}

α_R Heat transfer coefficient of the inner reactor wall in W m^{-2} K^{-1}

α_{Rad} Heat transfer coefficient of the outer reactor wall caused by radiation in W m^{-2} K^{-1}

β Thermal expansion coefficient of air in K^{-1}

φ_i Volumetric fraction of component i in −

δ_I Insulation thickness in m

δ_S Reactor wall thickness in m

ϵ_0 Emission coefficient of the thin aluminum layer in −

$\Delta G(T)$ Gibbs enthalpy as function of temperature in kJ mol^{-1}

Δh_R Enthalpy of formation for a certain temperature in kJ mol^{-1}

ΔH Enthalpy of formation at 298.15 K and 101,325 Pa in kJ mol^{-1}

$\Delta \dot{Q}(z)$ Heat losses along the reactor in W

λ Heat conductivity of air in W m^{-1} K^{-1}

λ_I Heat conductivity of the insulation in W m^{-1} K^{-1}

λ_S Heat conductivity of the reactor wall in W m^{-1} K^{-1}

v Kinematic viscosity of air in m^2 s^{-1}

ρ_S Catalyst bulk density

σ Stefan-Boltzmann constant in W m^{-2} K^{-4}

Δz Differential height element of the reactor in m

Latin Symbols a Reaction exponent for CO in -

A Cross section of the reactor in m^2

A_0 Outer reactor surface in m^2

A_i General inner cylindrical surface in m^2

A_I Mean logarithmic surface of the insulation in m^2

A_m General mean logarithmic surface in m^2

A_o General outer cylindrical surface in m^2

A_R Inner reactor surface in m^2

A_S Mean logarithmic surface of the reactor in m^2

b Reaction exponent for H$_2$O in −

c Reaction exponent for CO$_2$ in −

d Reaction exponent for H$_2$ in −

d_0 Outer reactor diameter in m

d_I Inner reactor diameter including reactor wall and insulation in m

d_R Inner reactor diameter in m

d_S Inner reactor diameter including reactor wall in m

E_a Activation energy in kJ mol^{-1}

Err Error in K

g Gravitational constant in m^2 s^{-1}

$GHSV$ Gas hourly space velocity in h^{-1}

Gr Grashof number in −

k_0 Rate constant in mol g^{-1} Pa$^{-(a+b+c+d)}$ s^{-1}

K Control variable for the finite difference approach in −

K_g Equilibrium constant calculated by thermo-physical properties in −

K_{MAL} Equilibrium constant calculated by the mass action law in −

$\dot{n}_i$ Molar flow rate of component i in mol s^{-1}

Nu Nusselt number in −

p Absolute pressure in Pa

p_i Partial pressure of component i in Pa

Pr Prandtl number in $-$

r Reaction rate in mol g^{-1} s^{-1}

R General gas constant in J mol^{-1} K^{-1}

R_Q Overall heat transfer conductivity in W K^{-1}

STDGR Steam to dry gas ratio in $-$

T Temperature in K

T_0 Ambient temperature in K

T_S Surface temperature of the thin Al layer of the insulation in K

$T_{c,i}$ Calculated temperature at thermocouple i in K

$T_{m,i}$ Measured temperature at thermocouple i in K

V_{Cat} Catalyst bulk volume in m^3

$\dot{V}_{Dry}$ Volumetric dry gas flow rate at STP in m^3 h^{-1}

$\dot{V}_{H2O}$ Volumetric steam flow rate at STP in m^3 h^{-1}

X_{CO} CO conversion in $-$

References

1. H. D. Baehr. Waerme- und Stoffuebertragung. Springer, 2013. doi: 10.1007/978-3-642-36558-4

2. Bohlbro H, Jorgensen M (1970) Catalysts for conversion of carbon monoxide. Chem Eng World 46:5–8

3. H. Bohlbro and E. Mogensen. An Investigation on the Kinetics of the Conversion of Carbon Monoxide with Water Vapour Over Iron Oxide Based Catalysts, 1969

4. Chinchen G, Logan R, Spencer M (1984) Water-gas shift reaction over an iron oxide/chromium oxide catalyst.: III: kinetics of reaction. Applied Catal 12(1):97–103. doi:10.1016/S0166-9834 (00)81507-9

5. Churchill S, Chu H (1975) Correlating equations for laminar and turbulent free convection from a horizontal cylinder. Int J Heat Mass Transf 18:1049–1053. doi:10.1016/0017-9310(75)90222-7

6. N. Diaz. Hydrogen Separation from Producer Gas Generated by Biomass Steam Gasification. PhD thesis, TU Wien, 2013

7. S. Fail. Biohydrogen Production Based on the Catalyzed Water Gas Shift Reaction in Wood Gas. PhD thesis, TU Wien, 2014

8. S. Fail, N. Diaz, F. Benedikt, M. Kraussler, J. Hinteregger, K. Bosch, M. Hackel, R. Rauch, and H. Hofbauer. Wood gas processing to generate pure hydrogen suitable for PEM fuel cells. ACS Sustain Chem Eng, 2 (12): 2690–2698, 2014. doi: 10.1021/ sc500436m.

9. Glavachek V, Morek M, Korzhinkova M (1968) Kinet Katal 9: 1107–1110

10. S. Hla, G. Duffy, L. Morpeth, A. Cousins, D. Roberts, and J. Edwards. Investigation of the effect of total pressure on performance of the catalytic water gas shift reaction using simulated coal-derived syngases. Catal Comm, 11 (4): 272–275, 2009. doi: 10.1016/j.catcom.2009.10.013.

11. S. Hla, D. Park, G. Duffy, J. Edwards, D. Roberts, A. Ilyushechkin, L. Morpeth, and T. Nguyen. Investigation into the performance of a Co-Mo based sour shift catalyst using simulated coal-derived syngases. Chem Eng J, 146 (1): 148–154, 2009. doi: 10.1016/j.cej.2008.09.023.

12. S. S. Hla, D. Park, G. Duffy, J. Edwards, D. Roberts, A. Ilyushechkin, L. Morpeth, and T. Nguyen. Kinetics of high-temperature water-gas shift reaction over two iron-based commercial catalysts using simulated coal-derived syngases. Chem Eng J, 146 (1): 148–154, 2009. doi: 10.1016/j.cej.2008.09.023.

13. Keiski RL, Salmi T, Niemisto P, Ainassaari J, Pohjola VJ (1995) Stationary and transient kinetics of the high temperature water-gas shift reaction. Applied Catal A: General 137(2):349–370. doi:10.1016/0926-860X(95)00315-0

14. Koppatz S, Pfeifer C, Hofbauer H (2011) Comparison of the performance behaviour of silica and olivine in a dual fluidised bed reactor system for steam gasification of biomass at pilot plant scale. Chem Eng J 175:468–483. doi:10.1016/j.cej.2011.09.071

15. M. Kraussler, M. Binder, S. Fail, A. Plaza, A. Cortes, and H. Hofbauer. Validation of a kinetic model for the catalyzed water gas shift reaction applying a Fe/Cr catalyst processing product gas from biomass steam gasification. In Proceedings of the 23rd European Biomass Conference and Exhibition, 2015

16. Kraussler M, Binder M, Fail S, Bosch K, Hackel M, Hofbauer H (2016) Performance of a water gas shift pilot plant processing product gas from an industrial scale biomass steam gasification plant. Biomass Bioenerg 89:50–57. doi:10.1016/j.biombioe.2015.12.001

17. Kraussler M, Binder M, Hofbauer H (2016) 2250-h long term operation of a water gas shift pilot plant processing tar-rich product gas from an industrial scale biomass steam gasification plant. Int J Hydorgen Energ 41(15):6247–6258. doi:10.1016/j.ijhydene.2016.02.137

18. B. J. McBride, S. Gordon, and M. A. Reno. Coefficients for Calculating Thermodynamic and Transport Properties of Individual Species. Technical report, NASA Lewis Research Center, 1993

19. Mueller S, Stidl M, Proell T, Hofbauer H (2011) Hydrogen from biomass: large-scale hydrogen production based on a dual fluidized bed steam gasification system. Biomass Conv Bioref 1(1):55–61. doi:10.1007/s13399-011-0004-4

20. Podolski WF, Kim YG (1974) Modeling the water-gas shift reaction. Ind Eng Chem Process Des Dev 13(4):415–421. doi:10.1021 /i260052a021

21. Rehling B, Hofbauer H, Rauch R, Aichernig C (2011) BioSNG-process simulation and comparison with first results from a 1-MW demonstration plant. Biomass Conv Bioref 1(2):111–119. doi:10.1007/s13399-011-0013-3

22. Rhodes C, Hutchings GJ (2003) Studies of the role of the copper promoter in the iron oxide/chromia high temperature water gas shift catalyst. Phys Chem Chem Phys 5:2719–2723. doi:10.1039 /B303236C

23. Rhodes C, Hutchings G, Ward A (1995) Water-gas shift reaction: finding the mechanistic boundary. Catal Today 23(1):43–58. doi:10.1016/0920-5861(94)00135-O

24. Sauciuc A, Abosteif Z, Weber G, Potetz A, Rauch R, Hofbauer H, Schaub G, Dumitrescu L (2012) Influence of operating conditions on the performance of biomass-based Fischer-Tropsch synthesis. Biomass Conv Bioref 2(3):253–263. doi:10.1007/s13399-012-0060-4

25. G. Smith. Numerical Solution of Partial Differential Equations: Finite Difference Methods. Oxford University Press, 3rd edition, 1985

26. M. V. Twigg. Catalyst Handbook. Manson Publishing, 1989.

27. www.scilab.org. Open source software for numerical computation, November 2015. URL www.scilab.org.

28. Zhu M, Wachs IE (2015) Iron-based catalysts for the high-temperature water-gas shift (HT-WGS) reaction: a review. ACS Catal 6(2):722–732. doi:10.1021/acscatal.5b02594